ACTA IMEKO
ISSN: 2221-870X
December 2026, Volume 15, Number 4, 1 - 7

Comparison of fracture energy of concrete under static and cyclic loading

Kamila Kozáková[1],Lucie Malíková[1], Vlastimil Bílek[2], Petr Miarka[1]

[1] *Institute of Physics of Materials, Czech Academy of Sciences, Žižkova 22, 616 00 Brno, Czech Republic*
[2] *VŠB — Technical University of Ostrava, Faculty of Civil Engineering, Ludvíka Podéště 1875/17, 708 00 Ostrava-Poruba, Czech Republic*

ABSTRACT
Fracture energy is the primary input for any cohesive analysis of concrete, yet it is almost always measured under monotonic static loading, while real structures are loaded repeatedly. This paper compares the fracture energy obtained from static three-point bending of notched concrete beams with the value derived from the envelope of low-cycle tests on nominally identical specimens of the same mix. Beams with relative notch depths a/W = 0.3 were tested on a servo-hydraulic machine, with the crack mouth opening displacement (CMOD) measured by a clip extensometer. The static work of fracture reached 258 J/m² up to a common CMOD of 0.42 mm, against 249 J/m² for the two low-cycle specimens, a difference of 3.4 %. The damage obtained from the unloading stiffness exceeded 0.9 by a CMOD of approximately 0.2 mm, while the irreversible CMOD grew linearly with CMOD at a slope of 0.88 to 0.92.

Section: RESEARCH PAPER

Keywords: fracture energy; concrete; damage; cyclic load

Citation: K. Kozáková, L. Malíková, V. Bílek, P. Miarka , Comparison of fracture energy of concrete under static and cyclic loading, Acta IMEKO, vol. 15 (2026) no. 4, pp. 1-7. DOI: 10.21014/actaimeko.v15i4.2505

Section Editor: Emina Hadzalic, University of Rijeka, Croatia

Received September 1, 2026; **In final form** November 9, 2026; **Published** December 2026

Copyright: This is an open-access article distributed under the terms of the Creative Commons Attribution 4.0 International License.

Funding: This work was supported Czech Science Foundation under project No. 25-15755S. No. CZ.02.01.01/00/22_008/0004631 *Materials and technologies for sustainable development* within the OP JAK programme.

Corresponding author: Petr Miarka, e-mail: miarka@ipm.cz mailto:paul@regtien.net

1. INTRODUCTION

The fracture behaviour of concrete has been studied systematically for around six decades, and the quantity that has proved most useful for describing it is fracture energy. Because an extended fracture process zone (FPZ) develops ahead of a traction-free crack, linear elastic fracture mechanics does not apply to laboratory-sized specimens. The material is described instead by the fictitious crack model, in which the FPZ is represented as a cohesive crack whose faces transfer a stress σ that decreases with the crack opening w [1]. The area under that softening relation is the fracture energy G_f, and no cohesive analysis of a concrete member can be carried out without it [2].

In the laboratory, G_f is obtained from the work of fracture: a notched beam is broken in three-point bending and the area under the measured load–displacement diagram is divided by the ligament area [3]. The procedure is simple, but the value it returns is not a material constant. It depends on the specimen size and on the notch depth, because the FPZ cannot develop fully close to a free boundary. Karihaloo and co-workers [4] addressed this by separating the measured, size-dependent energy from a size-independent value, which is recovered by combining tests on specimens with two different relative notch depths [5].

The fracture energy alone is not sufficient for a cohesive analysis; the shape of the softening relation $\sigma(w)$ is needed as well. A bilinear approximation is generally accepted as adequate for ordinary concrete, and its parameters can be identified inversely from a measured load–CMOD curve. Abdalla and Karihaloo proposed such a procedure based on the concept of a non-linear hinge [6], and Østergaard developed the cracked-hinge model into a closed-form solution for the complete load–CMOD response of a notched beam [7]. Because that solution is analytical, the inverse problem can be solved in seconds, and the identified law is consistent with the whole measured curve rather than with its peak alone.

Concrete structures are rarely loaded monotonically. Under repeated loading, the response of a notched beam departs from the monotonic one: every unloading–reloading cycle leaves a hysteresis loop and a residual crack opening, and the secant stiffness of successive cycles falls. Skar et al. extended the cracked-hinge model to cyclic loading, first for low-cycle damage

Table 1. Measured mechanical properties at 28 days of age.

Volume density ρ in kg m^{-3}	2432 ± 3
Compressive strength f_c in MPa	91.5 ± 4.3
Flexural strength $f_{c,t}$ in MPa	8.1 ± 0.4

in cemented beams on soil [8], and subsequently for fatigue crack growth [9]. Both formulations take the monotonic response to be the envelope of the cyclic one. That assumption is convenient, because it implies that the fracture energy of a cyclically loaded member could be recovered from a single monotonic test, but it is seldom checked directly against experiments on the same material and the same geometry.

The purpose of this paper is to make that check. Static and low-cycle three-point bending tests were carried out on notched beams cast from one concrete mix at two relative notch depths. The work of fracture is evaluated from the static load–CMOD curve and from the envelope of the low-cycle records, and the two are compared at a common crack opening. The damage is quantified from the unloading stiffness of each cycle and from the irreversible CMOD, and a bilinear softening law is identified from every record that reaches a complete softening branch. Because the whole comparison rests on the CMOD signal, the paper also documents the conditioning that the raw records require before any energy can be integrated from them–a step that is rarely reported, but that changed the fracture energy of one specimen here by almost 50 %.

2. EXPERIMENTAL DETAILS

This section gives an overview of the experimental and theoretical methods used in this study. The material, the test geometry, and the test procedure are presented, together with the evaluation of the fracture energy.

2.1. Material composition

An OPC based concrete was used for experimental testing. The mixture uses two fractions of aggregates, 0/4 sand and 8/16 high-quality crushed granite. Polycarboxylate based plasticizer was used to achieve better workability of the mixture. This mixture was mixed in a total of volume 0.2 m^3, and after demoulding, the samples were covered in PE foil to prevent excessive moisture exchange with the environment. The samples were kept in a laboratory with a controlled environment of 20 °C ± 1 °C. The measured mechanical properties are presented below in Table 1.

2.2. Fracture characterisation

Fracture properties are determined form the experimentally obtained work diagram or load–displacement curve. For concrete, this diagram shows a typical softening branch after the peak load, which results from energy dissipation in the FPZ [4].

Fracture test characterisation is done by evaluation fracture energy G_f, which is calculated as follows:

$$G_\mathrm{f} = \frac{W_f}{A_\mathrm{lig}}, \tag{1}$$

where A_lig is the ligament area and W_f is the work of fracture, that is the area under the load-CMOD diagram recorded during the fracture and low-cycle tests. The work of fracture can be calculated as follows:

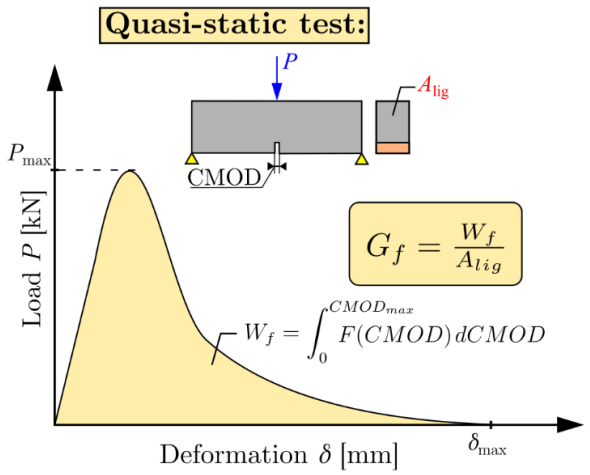


Figure 1: Schematic illustration of the fracture test of concrete.

$$W_\mathrm{f} = \int_0^{CMOD_\mathrm{max}} P(CMOD)\,\mathrm{d}CMOD, \tag{2}$$

where P is the measured load, $CMOD_\mathrm{max}$ is the maximum measured CMOD during the fracture test. This formulation provides information on the energy dissipation during the static fracture tests. The work diagram of concrete is schematically presented in Figure 1.

However, low-cycle testing uses the hysteretic loops to generate information on damage ω propagation [10]. The damage ω is calculated as change in the stiffness from each load step as follows:

$$\omega = 1 - \frac{E_i}{E_0}, \tag{3}$$

where E_0 is the initial elastic stiffness of the material, and E_i is the stiffness corresponding to i-th hysteresis loop of the load-CMOD curve. The schematic illustration of the low-cycle test is shown in Figure 2.

Additionally, the damage propagation within each load cycle is characterised by the irreversible crack mouth opening displacement $CMOD_\mathrm{IR}$. This parameter is the residual CMOD that does not recover upon unloading and appears once the elastic limit of the material is exceeded. In concrete, $CMOD_\mathrm{IR}$

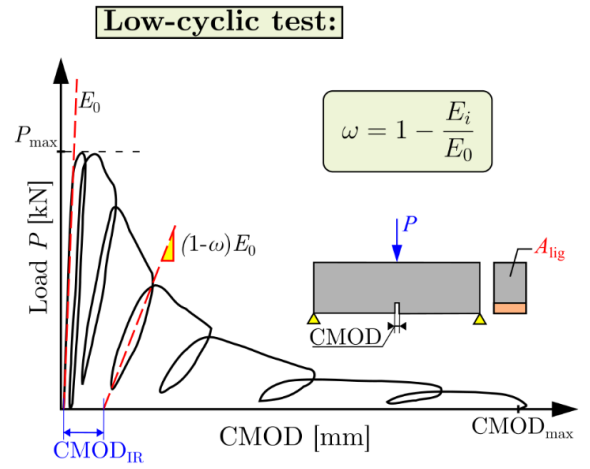


Figure 2: Schematic illustration of the low-cycle fatigue test.

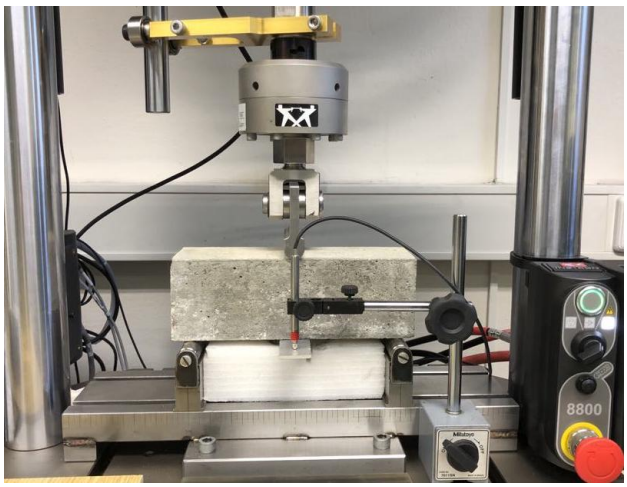


Figure 3: Experimental set-up of the three-point bending test with the clip extensometer mounted across the notch.

value arises primarily from the presence of the FPZ, rough ligament surfaces, and aggregate interlock across the crack, whereas for metallic alloys, $CMOD_{\mathrm{IR}}$ is attributed solely to plastic deformation and formation of plastic zone ahead of the crack tip.

The relationship between is assumed to act as the outer envelope of the low-cycle response. The work of fracture W_{f} and fracture energy G_{f} are therefore calculated from the envelope of the measured low-cycle deformation curve and compared with the values obtained from the static fracture tests.

2.3. Experimental set up and sample dimensions

For both static and fatigue experimental tests, a uniaxial servo-hydraulic testing machine Instron 8872 with a capacity of 25 kN (Instron, Great Britain) was used [11]. This system allows for CMOD-controlled experiments for static fracture tests, as well as force amplitude-controlled cyclic loading at frequencies up to 20 Hz. The experimental test setup is illustrated in Figure 3.

Data acquisition was done by two linear variable differential transformers (LVDTs), which were mounted on the specimen to measure mid-span deflection and CMOD values. The mid-span deflection δ was recorded using an LVDT with a measurement range of ± 10 mm and linearity within ± 60 µm (Micro-Epsilon Messtechnik, Germany). CMOD values were recorded using a high-precision COD extensometer, model Sandner EXR10-1O (SANDNER-Messtechnik GmbH, Germany), with a measuring range of 1 mm and an accuracy of ± 0.1 % and it was placed at the middle of thickness T. Both displacement measurements were synchronised with the applied load P throughout each test.

The low-cycle tests were applied as a sequence of 23 to 25 controller steps alternating between loading and unloading. The static tests were run in a single monotonic ramp. Both static and low-cycle experiments were performed in CMOD-controlled mode with a loading rate of 0.0025 mm/min. The unloading during the low-cycle loading started after predefined CMOD value for each load step derived from static test, and it was performed in force control mode with a loading rate of 0.0025 kN/min until a force of 0.05 kN was reached, then the loading step started.

In total, five samples were tested under two different loading conditions: static and low-cycle. The notch was cut by diamond saw with a thickness of approx. 2 mm. The initial notch length a_0 was 24 mm, providing a relative ratio of notch to height a_0/W of 0.3. This setup limits the brittle behaviour during the static monotonic loading. The measured dimensions of each sample are given in Table 2.

Table 2: Specimen dimensions; W is the height, T the thickness, and a_0 the notch length. The span was S = 200 mm for every specimen.

Sample	W in mm	T in mm	a_0 in mm	a/W	Loading
S1	78.88	45.04	23.56	0.299	static
S2	78.99	44.63	25.26	0.320	static
S3	79.25	45.18	23.72	0.299	static
T1	79.27	42.75	24.04	0.303	low-cycle
T2	79.38	42.25	24.24	0.305	low-cycle

3. DATA PROCESSING

3.1. Envelope and stiffness evaluation

The envelope of a low-cycle record was constructed from the virgin loading branch up to the peak load, followed by a monotone interpolation through the peak force of every subsequent loading step. The work of fracture of equation (2) was then integrated along that envelope.

The stiffness E_i of the i-th cycle was obtained by fitting a straight line to the upper 30 % to 90 % of the load range of each unloading branch. The lower part of an unloading branch is markedly curved once the specimen is damaged, and including it biases the secant. Branches with a coefficient of determination R^2 below 0.75 were rejected rather than reported. The reference stiffness E_0 was taken as the steepest sliding-window slope of the virgin branch, restricted to loads between 15 % and 70 % of the peak, which keeps both the seating of the specimen and the rounded peak out of the estimate. The irreversible opening $CMOD_{\mathrm{IR}}$ is the intercept of the same fitted line with the axis $P = 0$.

The elastic modulus was evaluated from the initial *P*–CMOD compliance of each specimen through the standard expression for a notched beam in three-point bending and varies between 26 GPa and 33 GPa for all five specimens.

3.2. Hinge model assessment

The tension-softening response was recovered from the measured *P*–CMOD records by inverse analysis with the non-linear cracked-hinge model, which confines the non-linear deformation to a band of width $s = H/2$ centred on the notch, while the remainder of the beam stays linear elastic [12]. Within the hinge, the closing tractions follow a bilinear law:

$$\sigma(w) = f_{\mathrm{t}} \cdot \max(1 - a_1\, w,\ b_2 - a_2\, w)\,, \tag{4}$$

from which:

$$\begin{aligned} w_1 &= \frac{1 - b_2}{a_1 - a_2},\ \ w_2 = \frac{b_2}{a_2},\ \ s_1 = b_2 - a_2\, w_1 \\ G_F &= \frac{1}{2}\, f_{\mathrm{t}}\, (w_1 + s_1\, w_2), \end{aligned} \tag{5}$$

where $\sigma(w)$ is the cohesive stress, f_{t} is the tensile strength, w is the crack opening, and a_1, a_2, and b_2 are bilinear coefficients. The crack opening w_1 corresponds to the inflection point of the bi-linear cohesive law.

The moment–rotation relation is available in closed form for each hinge state, so the complete *P*–CMOD curve follows analytically, and the inverse problem can be solved specimen by specimen.

Four softening parameters and the Young's modulus E were identified per beam. Because they govern distinct parts of the record, a Nelder–Mead search was run in three stages—E from the initial compliance, (f_t, a_1) around the peak, (a_2, b_2) from the tail—minimising the RMS load deviation, with openings admitting no equilibrium solution penalised rather than skipped, so that a truncated response could not be rewarded. Clip-gauge readings were referred to the notch mouth with a knife-edge offset $d_0 = 2$ mm. The fits reproduce the measured records to 1.4–3.8 % RMS of peak load.

The static beams were fitted over the complete monotonic record; for the low-cycle beams, the envelope through the peak of each loading step was used instead. Applying an identical procedure to both is what allows the envelope assumption to be tested: if the surrogate is faithful, the two parameter sets must be statistically indistinguishable.

4. RESULTS AND DISCUSSION

4.1. Load-CMOD response

The *P*-CMOD curves measured under monotonic static loading shows scatter in the maximum load P_{max}, which may be attributed to the highly heterogenous nature of concrete, where several mechanisms influence crack propagation. The curves exhibit the post-peak softening branch typical of quasi-brittle behaviour associated with the development of the FPZ. The measured work diagrams are shown in Figure 4.

The results of *P*-CMOD curves under the low-cycle tests show typical hysteretic loops with relatively low scatter in the obtained maximum load. With only two specimens, this agreement cannot be taken as evidence of material homogeneity. The experimental record of *P*-CMOD diagram under low-cycle load is shown in Figure 5.

In contrast to the static tests, the low-cycle tests were terminated at a lower CMOD, approximately 50 % of the value reached in the static tests. This reflects the extent of the prescribed loading programme rather than premature failure of the specimens.

An envelope curve was constructed from each experimental record and used as the input to the hinge-model identification. A comparison of the envelope curves is given in Figure 6.

The comparison of envelope curves provides information on the overall heterogeneity of the material. The differences in maximum load P_{max} are within acceptable range, as they show similar value of CMOD for load $P = P_{max}$. Additionally, this difference can be attributed to the different geometry of each specimen.

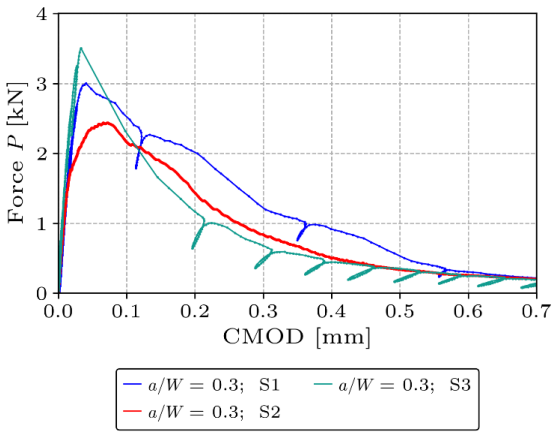


Figure 4: Load–CMOD curves of the static fracture tests.

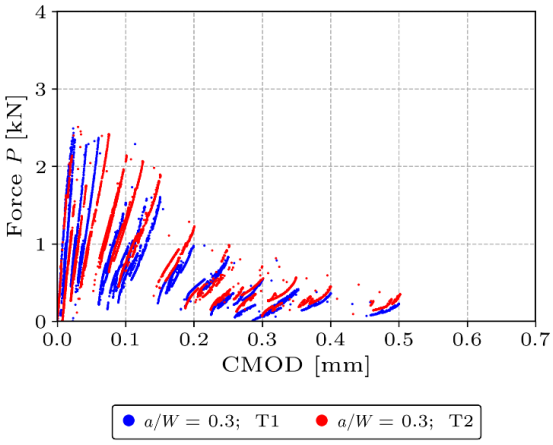


Figure 5: Load–CMOD curves of the low-cycle tests.

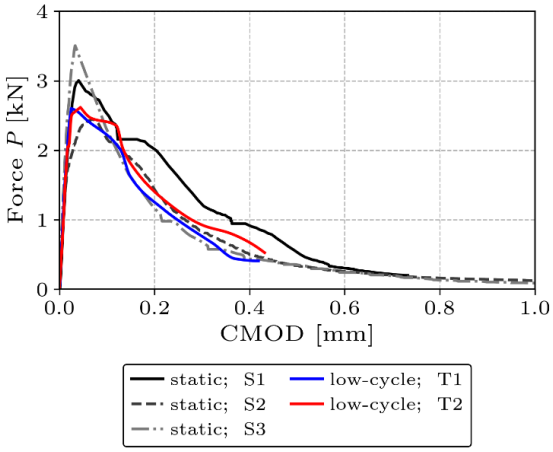


Figure 6: Comparison of envelope curves obtained from static and low-cycle tests.

4.2. Damage and irreversible crack opening

The stiffness degradation obtained from the hysteresis loops was used to calculate damage ω. The resulting damage evolution is presented in Figure 7.

The damage evolution follows the expected trend: ω increases with CMOD and is inversely related to the measured *P*-CMOD

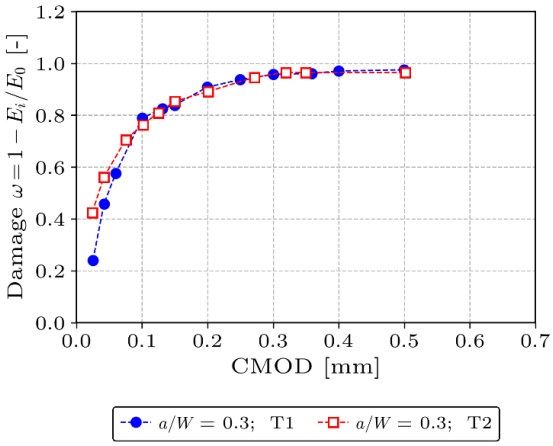


Figure 7: Identified damage propagation within the low-cycle test.

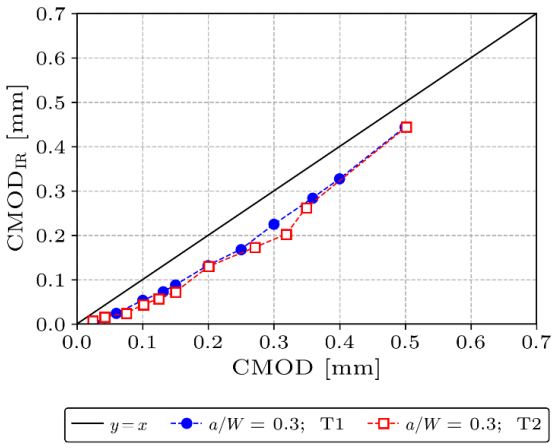


Figure 8: Identified $CMOD_{IR}$-CMOD relationship under low-cycle conditions.

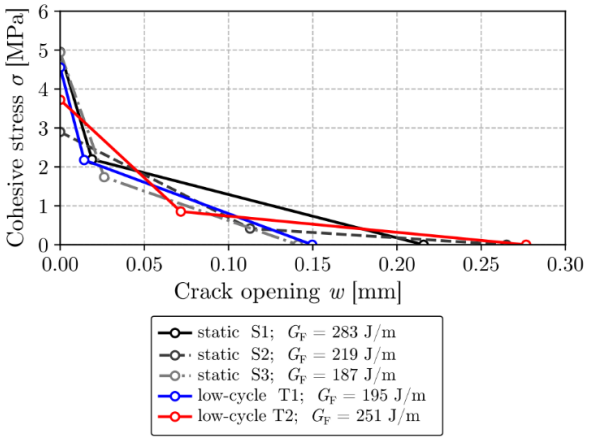


Figure 9: Identified bi-linear cohesive law parameter.

response. The two specimens give closely similar curves; although with only two records, this agreement should not be over-interpreted.

Such results can have practical implications in design of structure to seismic load or designing the foundations of heavy machinery.

A further parameter related to damage propagation is the irreversible opening $CMOD_{IR}$, which measures the accumulation of inelastic deformation and may be linked to the width of the FPZ. The $CMOD_{IR} - CMOD$ curves follow a similar trend for both specimens. The identified $CMOD_{IR}$ relationship is presented in Figure 8.

The $CMOD_{IR}$ relationship is almost linear, in contrast to the damage parameter ω described above. A linear fit gives a slope of 0.91 for T1 and 0.88 for T2, with an intercept of approximately −0.04 mm. We attribute this near-linearity to the growth of the FPZ and to the additional energy dissipated in each loading step.

4.3. Work of fracture and fracture energy

The work of fracture W_f and the fracture energy G_f can be obtained directly from the experimental *P*-CMOD record. The hinge model additionally yields a bilinear softening law, which converts the *P*-CMOD response into the σ-w relationship commonly required as input by commercial finite-element software for non-linear analysis [13]. The identified model parameters are given in Table 3.

In addition to the fracture parameters, the model identifies the tensile strength f_t and Young's modulus E, which describe the material response in tension.

The identified model's parameters show the change in the position of the $\sigma(w_1)$, i.e. inflection point of bilinear cohesive law. This change can be again related to the differences in the FPZ development during the test, different loading conditions, and to the typical heterogeneous features related to the concrete fracture, i.e. crack branching, aggregate bridging, and microcracking within the FPZ.

Similarly to the $\sigma(w_1)$, a difference in maximum crack opening w_u are identified. These differences are again with general expectation as the static *P*-CMOD curves generates longer tail, while the *P*-CMOD curves from the low-cycle tests have shorter tail due to repetitive loading steps. Identified maximum crack opening w_u under low-cycle loading conditions is in contradiction to the obtained $CMOD_{IR}$ and damage parameters ω. The identified parameters were validated to back calculate obtained *P*-CMOD curves with the error limited to 4 % in each identified work diagram.

The model's parameters are better visualised when plotting the bi-linear curves. In this sense, the clear differences or the similarities between each sample can be observed. The identified bi-linear cohesive law curves are presented in Figure 9.

The direct comparison between each test can be made by normalisation of cohesive law by identified tensile strength f_t. The differences are again clearly related to the loading type and consequent loading history. Such comparison is given in Figure 10.

The obtained values of fracture energy G_f for each loading are 230 J/m² and 223 J/m² for static and low-cycle tests, respectively. These nearly identical results are striking as the only envelope

Table 3: Comparison of hinge-model parameters.

Sample	f_t / Pa	E / GPa	a_1 / mm^{-1}	a_2 / mm^{-1}	w_1 / mm	$\sigma(w_1)$ / MPa	w_u / mm	G_f / J/m²	RMS/ %
S1	4.95	20.8	29.5	2.25	0.0189	2.19	0.216	284	2.4
S2	2.90	25.9	7.6	0.94	0.1128	0.42	0.265	219	1.4
S3	4.94	30.5	24.8	3.06	0.0261	1.74	0.141	187	2.2
T1	4.56	25.9	36.6	3.53	0.0142	2.18	0.150	195	2.9
T2	3.72	24.6	10.8	1.12	0.0716	0.85	0.277	251	3.8

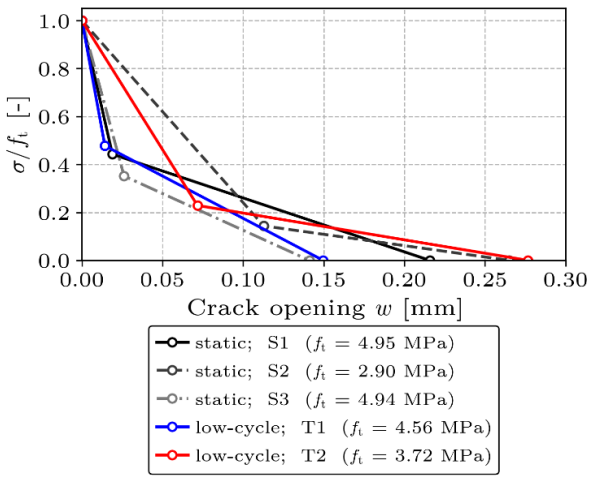


Figure 10: Normalised cohesive-law parameters.

Table 4: Average values of bi-linear cohesive law parameters for different loading conditions.

Sample	f_t / MPa	a_1 / mm	a_2 / mm	E / GPa	w_u / mm	G_f / J/m²
Static (n=3)	4.26 ± 1.18	20.6 ± 11.5	2.08 ± 1.07	25.7 ± 4.9	0.207 ± 0.062	230 ± 49
Low-cycle (n = 2)	4.14 ± 0.59	23.7 ± 18.3	2.32 ± 1.71	25.3 ± 1.0	0.213 ± 0.090	223 ± 40

curve used in the assessment of fracture parameters. The comparison of influence of load conditions on the loading parameters is shown in Table 4.

Average values of fracture energy G_f indicate similar values of energy dissipated during different loading conditions, however, when we identify progressive energy dissipation of each test, these similarities are limited to elastic behaviour of the material. The energy dissipation during the static and low-cycle test is shown in Figure 11.

The specific fracture energies obtained under the two loading conditions agree, once they are evaluated over a common crack opening. Because the low-cycle tests were terminated at a CMOD of approximately 0.4 mm, while the static tests were carried to 0.7—1.0 mm, all comparisons were made up to that common limit. On this basis, the static work of fracture G_f is 258 ± 36 J/m² against 249 J/m² for the low-cycle tests, a difference of 3.4 % and far smaller than the scatter between nominally identical specimens. Evaluating the static records over their full range gives a higher value simply because more of the softening tail is integrated, not because the material dissipates more energy under monotonic loading.

The inverse analysis leads to the same conclusion. The cohesive fracture energy G_f identified with the hinge model is 230 ± 49 J/m² for the static tests and 223 ± 40 J/m² for the low-cycle tests. Both the direct integration and the inverse identification therefore indicate that the envelope of a low-cycle record is an acceptable surrogate for the monotonic response for the purpose of fracture-energy assessment, within the resolution that the present number of specimens allows.

5. CONCLUSIONS

This study presents and discusses the application of envelope curve of the low-cycle loading test to the assessment of the fracture energy G_f. The results were compared against the static fracture behaviour obtained on the same material with same geometry of the sample. The *P*-CMOD envelope curve served as input to the hinge-model, which identifies the bi-linear cohesive law parameters of both low-cycle and static test.

The results show that the envelope curve can be used to identify fracture parameters, subject to the following limitations:

- The envelope neglects the energy dissipated within each hysteresis loop. That dissipation arises from crack-face friction and aggregate interlock rather than from new fracture surface.
- The low-cycle tests were terminated at CMOD 0.42-0.43 mm against 0.73-1.0 mm for the static tests. All comparisons were therefore made at a common cap of 0.42 mm.
- The low-cycle peak load is 12.5 % below the static mean, but damage from the cycles, the discrete sampling of the envelope near the peak, and specimen scatter cannot be separated with this data set.
- The hinge width $s = H/2$ and knife-edge offset d_0 = 2 mm were assumed rather than measured. G_f is robust to both (within 2 % and 4 %, respectively), but f_t shifts by 10–15 % with hinge width and is only weakly separable from a_1, so the branch parameters are model-dependent, and conclusions rest on G_f.
- The tests comprise a small number of cycles at increasing amplitude and are not high-cycle fatigue tests. The transferability of the identified parameters to high-cycle damage assessment remains to be verified.

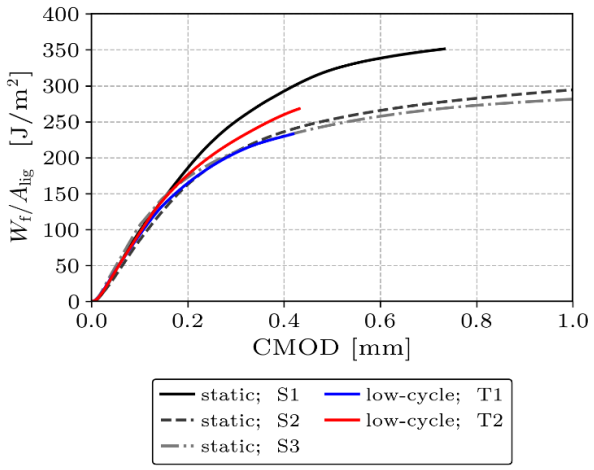


Figure 11: Comparison of fracture energy G_f dissipation during the static and low-cycle tests.

AUTHORS' CONTRIBUTION

Kamila Kozáková: investigation, data curation. Lucie Malíková: methodology, writing – review and editing. Vlastimil Bílek: resources, investigation, writing – review and editing, Petr Miarka: conceptualisation, methodology, investigation, formal analysis, writing – original draft.

ACKNOWLEDGEMENT

This paper was created as a part of project No. CZ.02.01.01/00/22_008/0004631 *Materials and technologies for sustainable development* within the OP JAK programme, co-financed by the European Union and the state budget of the Czech Republic, as well as the Czech Science Foundation under project No. 25-15755S.

During the preparation of this work, the authors used Claude Opus 5.0 (Anthropic, USA) in order to improve the readability, language of the manuscript, and data processing. After using this tool, the authors reviewed and edited the content as needed and take full responsibility for the content of the published article.

DATA AVAILABILITY

The data used in this study is available at: https://zenodo.org/doi/10.5281/zenodo.10390882.

REFERENCES

[1] B. L. Karihaloo, Fracture Mechanics and Structural Concrete, Longman Scientific & Technical, Harlow, 1995, ISBN 0470249889.

[2] M. Elices, G. V. Guinea, J. Gómez, J. Planas, The cohesive zone model: advantages, limitations and challenges, Eng. Fract. Mech. 69 (2002) 2, pp. 137-163.
DOI: 10.1016/S0013-7944(01)00083-2

[3] P. Miarka, L. Pan, V. Bílek, S. Seitl, H. Cifuentes, Influence of the chevron notch type on the values of fracture energy evaluated on alkali-activated concrete, Eng. Fract. Mech. 236 (2020), art. no. 107209.
DOI: 10.1016/j.engfracmech.2020.107209

[4] P. Nallathambi, B. L. Karihaloo, Determination of specimen-size independent fracture toughness of plain concrete, Mag. Concr. Res. 38 (1986) 135, pp. 67-76
DOI: 10.1680/macr.1986.38.135.67

[5] H. Cifuentes, B. L. Karihaloo, Determination of size-independent specific fracture energy of normal- and high-strength self-compacting concrete from wedge splitting tests, Constr. Build. Mater. 48 (2013), pp. 548-553.
DOI: 10.1016/j.conbuildmat.2013.07.062

[6] Abdalla, H. M., & Karihaloo, B. L., A method for constructing the bilinear tension softening diagram of concrete corresponding to its true fracture energy, Mag. of Conc. Res., (2004). *56*(10), pp. 597-604.
DOI: 10.1680/macr.2004.56.10.597

[7] Østergaard, L. Early Age Fracture Mechanics and Cracking of Concrete: Experiments and Modelling.Technical University of Denmark. 2003, BYG-Rapport No. R-070 ISBN 87-7877-133-1.

[8] Skar, A., Poulsen, P. N., Olesen, J. F., General cracked-hinge model for simulation of low-cycle damage in cemented beams on soil. Eng. Fract. Mech., *175*, (2017), pp. 324-338.
DOI: 10.1016/j.engfracmech.2017.01.016

[9] Skar, A., Poulsen, P. N., Olesen, J. F., A simple model for fatigue crack growth in concrete applied to a hinge beam model. Eng. Fract. Mech., 181 (2017), pp. 38-51.
DOI: 10.1016/j.engfracmech.2017.06.018

[10] A. Baktheer, H. Becks, Fracture mechanics based interpretation of the load sequence effect in the flexural fatigue behavior of concrete using digital image correlation, Constr. Build. Mater. 307 (2021), art. no. 124817.
DOI: 10.1016/j.conbuildmat.2021.124817

[11] P. Miarka, J. Ríos, L. Malíková, V. Bílek, Fatigue resistance of concrete revisited: Wide range data from low-cycle to high-cycle and influence of aggregate on fatigue lifetimes, Cem. Concr. Compos. 166 (2026), art. no. 106394.
DOI: 10.1016/j.cemconcomp.2025.106394

[12] Y. Jenq, S. P. Shah, Two parameter fracture model for concrete, J. Eng. Mech. 111 (1985) 10, pp. 1227-1241.
DOI: 10.1061/(ASCE)0733-9399(1985)111:10(1227)

[13] J. D. Ríos, H. Cifuentes, C. Leiva, S. Seitl, Analysis of the mechanical and fracture behavior of heated ultra-high-performance fiber-reinforced concrete by X-ray computed tomography, Cem. Concr. Res. 119 (2019), pp. 77-88.
DOI: 10.1016/j.cemconres.2019.02.015